# INVESTIGATION OF DEFECT FORMATION AND CONTROL IN POLY-CRYSTALLINE ANATASE TITANIUM DIOXIDE

BY

DAVID EITAN BARLAZ

THESIS

Submitted in partial fulfillment of the requirements
for the degree of Master of Science in Chemical Engineering
in the Graduate College of the
University of Illinois at Urbana-Champaign, 2013

Urbana, Illinois

Adviser:

Edmund G. Seebauer

## ABSTRACT

Titanium dioxide ($TiO_2$) has become one of the most prominent materials in the research efforts related to the clean production of energy and value added chemicals. $TiO_2$ has been praised for the catalytic activity of its anatase phase, its abundance in nature, low toxicity, stability in aqueous environments and ease of processing. Among its drawbacks is a high native carrier concentration likely due to the formation of oxygen vacancies and their clustering at grain boundaries which impede hole mediated photocatalytic reactions[1]. Previous efforts to defect engineer atomic layer (ALD) grown $TiO_2$ were successful by varying film thickness, with the explanation that films differentially compacted during annealing according to thickness leading to less area at grain boundaries for defects to aggregate[2].

We sought to further that success by several methods. Lowering growth rate and increasing synthesis temperature sought to lower carrier concentration by increasing surface mobility of deposited atoms increasing the density of unannealed films. Varying the ramp rate used in annealing was also performed to test for variations in crystallite formation and growth with the goal of producing larger grains with reduced net interfacial area for defects to aggregate.

The methods of increasing surface mobility each had the effect of lowering carrier concentration by about ½ an order of magnitude. Short range order in the form of subcritical nuclei was suggested as an explanation. The presence of such order had already been observed during surface diffusion experiments on amorphous titanium dioxide[3]. Subcritical nuclei present in the bulk of an amorphous film are the first to grow upon annealing possibly crowding out newly seeded nuclei thereby increasing the average crystallite size and film density. Their increased production by

increased surface mobility and increased growth time (thickness in the previous work) led to denser films and lower carrier concentrations. The critical point in the annealing process for their growth and for the formation of new nuclei was not able to be determined as variations in ramp rate led to no appreciable variation in carrier concentration. This suggested that the critical temperatures are close to the annealing temperature or that the time scale for this production is shorter than that accessed by rapid thermal annealing.

## ACKNOWLEDGMENTS

בס"ד

I'd like to thank first and foremost my advisor as well as lab mates past and present for training, advice, and support through the years. Akin to my lab are many collaborators and equipment superusers throughout the university. In particular I'd like to single out Dane Sievers for encouragement, training and a great number of stimulating discussions as I made my way into the field. Thanks to Mauro Sardela for training and help interpreting X-Ray data, Julio Soares for spectroscopic ellipsometry, and Hal Romans for the Sputterer and furnace training.

Thanks to all the friends (both UD and UI based) and family for keeping me sane over the years with of course a special shout out to my fiancé Marissa Goldrich. Just a few more months dear, then we'll be married. Many guys to thank, not nearly enough room here, but I'd be remiss if I did not at least include Brian Rosen, Ilan Cohn, Aaron Reinicker, and Kevin Brew. I do not know what I would be without you guys.

## TABLE OF CONTENTS

## LIST OF FIGURES

# Chapter 1

# INTRODUCTION

## 1.1 Defect Engineering

Defect Engineering formed the basis for the birth of microprocessors as it was discovered that many transistors could be fabricated on a chip with a density many orders over that of a tube transistor device. The term 'defect' in a crystalline material can encompass a huge variety of types ranging from point defects in a crystal lattice caused by the removal, translation, or addition of either a native or foreign atoms to clusters of defects as shown in Figure 1[2].

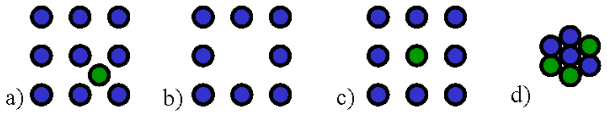


**Figure 1: Examples of interstitial (a), vacancy (b), substitutional point defects (c) and defect clusters (d).**

The foundation for defect engineering was that the conductivity, resistivity, capacitance, and other electronic properties of crystalline materials could be precisely tuned by controlling the type and/or concentration of non native defects in the material.

In the case of early computer chips, the primary crystalline material used was Silicon. The invention of the Czochralski process to produce low cost, highly single crystalline, high purity silicon wafers led the majority of defect engineering efforts to focus on the introduction of foreign atoms (dopants) both during growth and

later via high energy ion implantation. Current defect engineering efforts in silicon on the side of single crystal purity work includes annealing procedures to remove low level carbon-oxygen complexes[4]. Advanced ion implantation research includes a crystalline-to-amorphous transformation to lower the energy required for ion implantation[5], as well as efforts to apply ion implantation techniques to new silicon structure such as nanowires[6].

Since then, the field has expanded to include both single- and polycrystalline. As will be seen, the methods used to control defect concentration similarly expanded to include not only the addition of dopants as a post growth processing techniques, but other processing steps such as *in situ* doping, other growth controls, annealing, etc. As with silicon, there is a lot of interest in doping non-traditional structures such as nanowires, but the geometry and surface shape creates numerous difficulties including a crystalline-to-amorphous transformation. Attempts have so far been made to dope GaAs and ZnO nanowires with both transition and rare earth metals, for use in spintronic and luminescence devices[6]. Ion implantation for improved luminescence properties has been similarly sought in other materials used in light emitting diodes (LEDs) such as GaN[7].

In a similar effort to move away from Silicon as a base material for new generations of electronic devices, defect engineering efforts have also been made in graphene sheets. Annealing under controlled atmospheres has already been used to remove oxygen based defects[8]. Research on controlled irregular defect shape in graphene by computational simulation has also reveled that ability for triangular defects to act as a thermal rectifier similar in principle to and LED but for thermal energy[9].

Defect engineering in other metal oxides has also grown. In addition to ZnO, defect engineered $HfO_2$ has been under investigation as a possible magnetic semiconductor for use in memory devices. In the case of $HfO_2$, the switching speeds of memory units are closely correlated to concentrations of oxygen vacancies[10]. $TiO_2$ research is likewise ongoing for photocatalytic systems. In addition to its native n-type forms, recent research has demonstrated producing p-type material via titanium interstitial creation under an oxygen atmosphere[11].

### 1.2 Titanium Dioxide

The material of choice for our defect engineering investigations in Titanium Dioxide ($TiO_2$). There is a constantly growing body of literature surrounding $TiO_2$ since the discovery of its photocatalytic properties[12]. It is under investigation for use throughout materials research as a photocatalyst, other areas of heterogeneous catalysis, as well as a catalyst support. It is stable in a number of typical operating environments being highly insoluble. It is inexpensive to obtain, and benign to both humans and the environment. Specifically, we hypothesize that $TiO_2$ can become a more viable catalytic material with principles of defect applied to its growth and processing to control carrier concentration. Once the production of the material is developed in such a manner, desired carrier concentrations can be tuned to individual reactions or processes. For example, in the case of certain photocatalytic systems, lowering carrier concentration is a means to increase carrier lifetime which is key to improved quantum yield[1].

Despite the immense interest and investment in $TiO_2$ development as a catalyst, a great deal remains to be investigated. In its native anatase form, it is highly n-type with an electrically active carrier concentration of about $1*10^{17}$ charges/$cm^3$. It

also exhibits several polymorphs or varying catalytic activity with the more active being the kinetically favorable but thermodynamically unstable anatase phase. When exposed to temperature above about 700 °F, the more thermodynamically favorable rutile phase begins to form[13].

A variety of substitutional defects have been successfully incorporated by various groups with varying success in altering reaction rates in test systems[1]. Substrate choice has been shown to affect catalytic activity[14]. Other reports demonstrate the varying of morphological properties with variations in synthesis and processing which are similarly correlated to changes in reaction rate[15-19]. There exists a great gap however in the literature of reliable measurements of carrier concentration, especially in same studies which attempt to explain improvements in a desired reaction rate with alterations in microstructure.

### 1.3 Short Range Order

While the microstructure of a polycrystalline film is complex in itself, there is also another regime of crystallinity that must be accounted for when studying the crystallization of an amorphous material. Typically, crystallinity in films is detected by spectroscopic techniques such as X-Ray Diffraction as will be discussed later. This technique can produce a lot of noise especially with films with significant surface roughness meaning that the smallest crystal detectable will be on the scale of several to tens of nanometers containing dozens to hundreds of unit cells. Many nominally amorphous materials contain a shorter range crystallinity that forms under growth conditions but is not detectable by commonly available spectroscopic methods. This level of order is not necessarily energetically stable over long periods of time. However, if a nominally amorphous film begins crystallization soon after growth, this

short range order may allow nuclei for larger stable crystallites to form more quickly. This regime of crystallinity has been given several different terms in the literature, several of which are introduced below. For simplicity, in subsequent sections of the present work this regime of crystallinity will be collectively referred to as "short range order".

Nanoscale order in the form of "subcritical nuclei" in amorphous titania-silica glass has been detected using neutron scattering data assisted by computational techniques[20]. Experimental techniques have been developed for detecting nanoscale order using Fluctuation Transmission Electron Microscopy[21] in some disordered solids with some complimentary computational work[22] by the Abelson group at U. of Illinois.

The presence of "medium range order" in the form of subcritical nuclei in CVD-deposited amorphous $TiO_2$ was noted by our group in a photo-assisted surface diffusion experiment[3]. Here subcritical nuclei were present throughout an amorphous titania film, and the film was exposed to low level UV light through a patterned photo mask. In areas exposed to the light, critical nuclei grew as mobile surface atoms migrated to the subcritical nuclei. Furthermore, the shape of the final crystallite was controllable by varying the pattern of the photo mask.

If the same level of short range order detected at the surface by Kondratenko *et al.* is present in the bulk of our amorphous titania films, it may have a noticeable effect on the final crystallized form.

### 1.4 Primary Goal: The control of carrier concentration in $TiO_2$

The production of defect engineered $TiO_2$ would enable a new class of catalytic materials to enter the market. The native carrier concentration is high such that drift and diffusion currents of newly generated carrier are in competition. Ideally,

electron-hole pairs would be separated by charge with electrons being swept the surface to participate in a reaction. When diffusion current, and carrier recombination rates, dominate the drift current a lower reaction rate is observed. Lowering of the native carrier concentration allows for the drift component of generated carriers to dominate delivering more charge to the surface where it is needed[1].

Our goal is therefore to control the carrier concentration in $TiO_2$ over as great a range as possible, with a specific desire to decrease from the native value. Subsidiary to that, we also wish to do so without the use of dopants. Dopants (via substitutional defects) introduce a large set of subtle variables into the production process and overall increase the hazards of the process via toxicity.

Additionally, we would like to investigate the stability of the $TiO_2$ we produce. Thin films, like any other crystalline material, can experience aging for a variety of reasons. While a kinetically stabile phase would be expected to retain morphological and electronic properties for extended periods of time, that time is crucial for experiment planning as well as provides information about expected lifetime of a defect engineered product brought to market.

### 1.5 Hypothesis

There is good evidence that the primary source of intrinsic negative charge in $TiO_2$ is brought about by the formation of oxygen vacancies in the bulk, and the clustering of their released charges at grain boundaries, or other morphological discontinuities. We hypothesize that this charge build up could be prevented, or at least limited, by the lessening of grain boundary formation as seen by film densification and crystallite size.

# Chapter 2

# EXPERIMENTAL METHODS

## 2.1 Synthesis

$TiO_2$ can be synthesized into thin films by a wide variety of methods. The most popular within the Integrated Circuit (IC) industry is by some type of Chemical Vapor Deposition (CVD). $TiO_2$ used as an anti-reflective or photocatalytic glass coating is usually deposited using a sol-gel method to minimize cost. In the later application, film properties beyond stability in water or organic residue are largely unimportant. In the former, tight control over morphology, crystallinity, and electronic properties is desired. As a result, techniques adapted from the IC industry are most applicable to defect engineering efforts in thin films.

### 2.1.1 Atomic Layer Deposition

Atomic Layer Deposition (ALD) represents a sub-set of CVD techniques. In both cases, a synthesis chamber is fed gas phase precursor(s) at controlled rates. The chamber is operated in vacuum to prevent contamination or unintentional doping of the film. The primary difference between CVD and ALD is that the former delivers multiple precursors simultaneously to the chamber with deposition time and sample temperature being the only controllable growth variable. CVD also has the disadvantage of less uniform coverage due to lower surface mobility of deposited atoms[23]. ALD by comparison, is a layer-by-layer, self limiting growth technique in

which the precursors are fed to the chamber in individual alternating pulses with a purge between each pulse. By allowing each precursor to decompose entirely and allowing byproducts to be pumped away, the growth is self limited by the amount of precursor delivered by the pulse. In true ALD, pulses and purges are timed such that the growth is a single atomic layer or less per pulse ensuring uniform film growth. In the case of crystalline or epitaxial film growth, this helps to ensure a highly crystalline product. When synthesizing amorphous films, the low growth rates are not inherently required for the process, and pulses can be increased to produce growth rates of several nm/cycle in a pseudo-ALD layer-by-layer technique. In this way, growth rate becomes a controlled variable during synthesis as well.

### 2.1.2 $TiO_2$ Precursors

When using a CVD technique, there are several popular titanium bases precursors which can be used. Two of the commonly used ones earlier in the days of $TiO_2$ research were $TiCl_4$ and $TiF_4$. Both can be delivered as compressed gases to the chamber in a controlled manner, but they have several distinct disadvantages. Both are highly corrosive and will damage even stainless steel chambers over time. Iron is one of many elements which has been used as a thin film dopant, so it is important to avoid its accidental introduction into the sample. Vacuum pumps maintaining chamber pressure will also be similarly corroded. Both precursors are also highly toxic to humans, so if their use can be avoided, it greatly reduces the number of engineering controls needed for safe operation.

The current precursor of choice is titanium tetra-isopropoxide (TTIP), shown in Figure 2. Though a liquid at room temperature, TTIP produces an

appreciable vapor pressure according to Equation 1 when heated[24], and can thus be delivered to the chamber via a carrier gas such as $N_2$.

$$\log(P_v)[\mathrm{Torr}] = 9.465 - 3222/T[\mathrm{K}] \qquad \text{(Equation 1)}$$

**Equation 1: Vapor Pressure of TTIP**

Though it degrades slowly with time and exposure to light, it is stable in the absence of moisture. It is unique among many metal organic precursors as it has multiple decomposition pathways depending on temperature and the choice of oxidizing agent as a 2nd precursor.

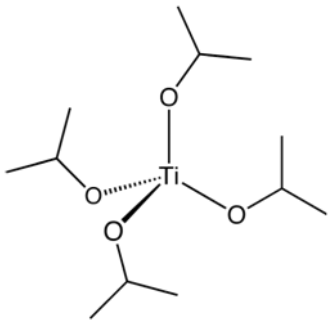


**Figure 2: Structure of TTIP - $Ti(OC_3H_7)_4$**

TTIP will decompose upon heating above about 100 °C without such an agent though higher temperatures (above ~165 °C) are favored for TTIP decomposition to avoid unoxidized carbon contamination of the sample[25, 26]. The use of an oxidizing agent is the simplest method for eliminating carbon; others have avoided it by using an evaporated Ti layer to begin deposition rather than expose Si to the TTIP directly[27]. Oxidizing agents can be selected based on synthesis temperature, but selection rules are flexible. Common agents include $O_2$ gas, and $H_2O$ or $H_2O_2$ fed by a carrier gas from a bubbler. Water has limited reactivity below 150 °C[28], but above that it is a good agent as it is insensitive to temperature[29], safe to use, and easy to provide in excess leaving TTIP as a limiting reagent. TTIP will decompose above about 100 °C

to produce propane and water without an oxidizing agent making water the lower limiting factor in regards to deposition temperature.

Conversely to water, TTIP has an upper limit as far as deposition is concerned. Above about 300 °C, the decomposition product shift to include more isopropanol and eventually to propene[25, 30]. This shift coincides with the precursor sticking to adsorption sites. Lowering surface mobility in this way prevents true self limiting growth necessary for ALD. Additionally, the rapidity of the decomposition precludes an oxidizing agent being able to participate due to the purge time. Above about 340 °C, TTIP will begin decomposition in the gas phase especially when not shielded from self collisions by a carrier gas[31].

### 2.1.3 Sample Preparation

Thin films require a substrate for growth. In the case of amorphous or polycrystalline films, the substrate does not need to have any lattice matching with the thin film as would be required for epitaxial monocrystalline growth. Silicon (Si) is commonly used for such research work given it's high thermal stability. Silicon also has the advantage or glass of being opaque to lasers used in ellipsometry as well as being conductive enough for use in electrical testing of the thin film as will be discussed later.

Antimony doped Si(100) wafers (Silicon Quest International) with n-type resistivity of 0.013 Ω*cm were cut into 2*2 cm squares for use as thin films substrates. These chips were degreased by successive rinsing in acetone, isopropanol, and acetone before drying with compressed air. With any organic residue removed, chip were then etched in 48% HF (Sigma Aldrich) (1 min) and rinsed in deionized water (1 min) to remove the native $SiO_2$ layer that otherwise acts as an undesired insulator. Chips are

loaded immediately into the vacuum chamber after drying with compressed air to avoid allowing the $SiO_2$ to regrow.

### 2.1.4 Chamber Specifications

The chamber used for CVD/ALD is a stainless steel chamber with a six way cross. The chamber is Teflon (Dupont 852-202, 850-799) coated to prevent reactions with the chamber walls and/or other types of contamination. The chamber is pumped to a base pressure of approximately 50 mTorr by a Varian SD200 direct drive pump with a nominal operating pressure of 200 mTorr. Pressure is monitored by a 0.1 Torr scale MKS Baratron capacitance manometer. Exhaust lines for water and TTIP are pumped by an oil-sealed belt drive Welch 1405 and a direct drive Alcatel 2010SD respectively.

The sample platform was custom built to house a 150 W halogen bulb (Osram 24V GY6.35). The bulb is powered by a Variac power controller while a chromel-alumel (type K) thermocouple soldered to the sample platform monitors temperature.

The chamber is set up to handle the delivery of 2 independent precursor gas streams. Here, TTIP (Strem Chemicals Inc., 98%) and $H_2O$ (DI, no further purification) are delivered in a carrier stream of 20 psi $N_2$ gas (SJ Smith, 99.999%). A flow rate of 60 SCCM by MKS 1179A Mass Flow Controllers (MFCs) and a MKS 247D 4-Channel Readout. The TTIP bubbler is heated by a water bath to 60 °F, which is preceded by a cold trap to ensure that any vaporized TTIP not moved downstream can not make its way upstream to the MFC. The water bubbler is allowed to stay at room temperature and mixes water into the gas stream by way of sparging the $N_2$ though it.

Pulse/purge timing is controlled by a custom written Labview program and associated Labjack U12 units which operate a set of four pneumatic valves (Swagelok SS-BNV51-C) via a custom made electronic air handling manifold (Compressed air, 60 psi). Two valves sit on branches of the gas delivery lines. One outlet goes to the chamber, with the other going to the exhaust pump. Exhaust valves are nominally open and chamber valves shut except during precursor pulses. This design allows for continuous gas flow through the bubblers reducing pressure spikes in the chamber.

### 2.1.5 Ellipsometry

Upon completion of growth, film thickness and uniformity are determined using a Rudolph Technologies AutoEL II Ellipsometer. It is a single wavelength ellipsometer that uses a 0.2 mW HeNe laser (632.8 nm) impinging on the sample surface at 45° with the reflection hitting a detector opposite the laser mount. From a given refractive index the pre-programmed routines will determine a film thickness with accuracy of about 1 nm. A separate program can be used to determine refractive index and thickness simultaneously, but with reduced accuracy. Nominal film uniformity from our pseudo-ALD growth process, as estimated by thickness measurements about ½ cm apart, is about 1% of film thickness.

### 2.1.6 Annealing

Synthesized films can be amorphous or polycrystalline depending on synthesis temperature. Most amorphous films are annealed in a tube furnace (Barnstead Thermolyne F79300) under an ambient atmosphere. The programmable furnace allows films to be annealed at a specified ramp rate for specified time before

turning off and allowing samples to cool. This furnace was capable of ramp rates up to approximately 60 °C/min.

For faster ramp rates, a rapid thermal processor (Jipelec JETfirst RTP) capable of 20 °C/s was also used. The Jipelec uses a series of Halogen bulbs behind quartz window as a heat source. The instrument's manual says the bulbs are designed to emit primarily in the infrared (IR); halogen bulbs typically have a broad emission spectra including the UV which may have an effect on $TiO_2$ film crystallization[3]. The quartz window was used for even heating and not for UV filtration. Because rapid thermal processors are not capable of sustaining hold temperatures for more than a few minutes, longer anneals were carried out in an adjacent tube furnace (Lindberg/Tempress Model 8500) also under an ambient atmosphere.

## 2.2 Morphological Characterization

While a single wavelength Ellipsometer is sufficient for films of known refractive index, it becomes a tool of limited value for polycrystalline thin films. Polycrystalline films tend to have varying refractive index, and even a small change (1%) can introduce significant inaccuracy to thickness measurements. In addition to more accurate thickness measurements, other morphological data for thin films is typically learned through the use of non-destructive X-ray based techniques.

### 2.2.1 X-ray Reflectivity & Refractivity

Morphological data were acquired through the use of a PANalytical X-ray difractometer. The Copper X-ray source operated at 45 kV and 40 mA. The detector was a PIXcel High Speed Line detector capable of 25 million counts per second per

strip. For X-ray Reflectivity scans, a 1/32 degree slit is used with the divergence slit, X-ray diffraction scans use a 1/2 degree slit.

X-ray reflectivity (XRR) data were analyzed for bulk density as well as thickness. Density was determined one of two ways depending on the quality of the scan. The most direct method is as follows[2]. The experimentally determined critical angle of total external reflection, $\theta_c$, is related to the bulk density of the film $\rho$ according to Equation 2. $\theta_c$ is obtained from the angle at which the XRR spectral intensity is half of the plateau value[32].

$$\frac{\theta_c^2}{\rho} = \frac{r_e \lambda Z N_A}{\pi A} = F \qquad \text{(Equation 2)}$$

**Equation 2: Density as a Function of Critical Angle**

$F$ is constant for a given material and irradiating beam. From literature sources, $r_e$ is the classical electron radius ($2.82*10^{-15}$ m), $\lambda$ the x-ray wavelength, $Z$ the atomic number, $N_A$ Avogadro's number, and $A$ the mass number[33].

PANalytical X-ray Reflectivity software package can also determine density and thickness through a simulation method where the two parameters along with surface roughness are varied by the user to match the experimental data. In cases where simulation was used, the stack used was $Si/TiO_2$ with a surface roughness of about 1 nm.

X-ray diffraction (XRD) data were analyzed using MDI JADE software. Peak identification was done using JCPDS cards 21-1272 and 21-1276 for anatase and rutile phases respectively. Scherrer's formula (Equation 3) is used by the software to

$$D = \frac{0.9\lambda}{B\cos(\theta)} \qquad \text{(Equation 3)}$$

**Equation 3: Scherrer's formula**

determine individual crystallite sizes. From the instrument, $\lambda = 0.15406$ nm. Additionally, $\beta = B - b$, where $B$ is the observed FWHM and $b$ is the instrument function determined from the broadening of the monocrystalline silicon diffraction line. Peak broadening was assumed to be solely a function of crystallite size as microstrain and temperature effects are expected to be negligible for room temperature measurements[2].

Without a more direct visualization method, determination of grain size is not possible. Crystallite size is therefore used as a type of proxy for grain size with the assumption that they are at least partially correlated.

### 2.2.2 Spectroscopic Ellipsometry

While XRR remains the most authoritative method of determining thickness, scan times can be lengthy. If only thickness information is desired, but refractive index is not reliably known, spectroscopic ellipsometry can be employed as an alternative. However, it is more sensitive than XRR to substrate type in that transparent substrates can reduce accuracy.

Scans of polycrystalline films of unknown refractive index were obtained using a J. A. Woollam Co. variable-angle spectroscopic ellipsometer. The ellipsometer is comprised of a polarizer, and rotating angle sample mount, and a second polarizer with two photo detectors covering a range of 240 to 1700 nm. The detectors determine the change in polarization of light relative to the incident linearly polarized beam relative to the angle of incidence on the sample. A least square fit method fits the data to simulated data based on a model of the physical sample to obtain thickness and refractive index data[i].

[i] Thanks to Julio Soares for help with this description.

Scan data from the spectroscopic ellipsometer is not shown in this document. It's description was included because it was used to confirm the unreliability of the single wavelength ellipsometer for polycrystalline film measurements and to test for significant changes in refractive index between films that could become important if interfacial studies of polycrystalline samples were to be carried out in the future.

### 2.3 Electrical Characterization

Defect engineering desires to control the concentration of electrically active defects in a material. This is a non-trivial matter in $TiO_2$ and indeed much of the literature seeks to explain catalyst performance solely in terms of morphological properties as a work around. $TiO_2$ has a relatively high bandgap (3.2 eV), and forms a Schottky diode with many metals. This makes Hall effect measurements difficult, and traditional Four Point Probe (4PP) measurements nearly impossible.

To overcome this, carrier concentration is derived from Mott-Shottky plots taken from Capacitance-Voltage sweeps of $TiO_2$ thin films built into an electrical circuit with the metal contacts and the silicon substrate. The device structure and protocol largely matches a related one developed previously in this research group[2, 34] except that the contact to the silicon substrate was changed from InGa to aluminum. The switch was made following the observation that aluminum sputtered onto abraded silicon formed an ohmic contact of similar resistance to the InGa/Si contact despite the abraded silicon being exposed to air for a longer period of time before the contact was laid down. The switch reduced processing steps as well as removed the use of eutectic InGa which is hazardous.

### 2.3.1 Schottky Diode fabrication

In order to carry out electronic testing of $TiO_2$ films, the film must be built into a complete device with the $TiO_2$/metal interface forming a diode with all other interfaces being ohmic and of minimal resistance. Aluminum forms a Schottky diode with $TiO_2$ surface[34] and an ohmic contact with n-type Silicon[35].

The device was fabricated with abrading a corner of the $TiO_2$ film with fine sandpaper until bare silicon was exposed. With both silicon and $TiO_2$ exposed, contacts could be fabricated simultaneously via photolithographic patterning. Samples were degreased in acetone, dried, before being coated with positive photoresist (Shipley Megaposit SPR 220-3.0). Spinning at 4500 rpm (acceleration 1500 rpm/s) for 30 seconds provided a uniform coating of approximately 4 μm. The coating was prebaked at 110 °C for 90s before circles of $2.0*10^{-3}$ $cm^2$ were degraded using a Karl Suss MJB3 Contact Mask Aligner with a photo mask made by university printing services. Exposure was 9 $mW/cm^2$ for 45 seconds. Samples were hardbaked at 110 °C for 90s before being developed (Shipley MF-24A).

Sputtering of Al contacts was done in a Cooke Dual-Gun Sputter System with an Al target with a base pressure of about $1*10^{-5}$ torr after one hour of high vacuum pumping. Sputtering was done at 200 W under 8 SCCM of Argon. A sputtering time of 6 minutes gives a coating of about 200 nm. Photoresist liftoff was done by sonicating in acetone before drying with compressed air. A schematic of the final device can be seen in Figure 3[2].

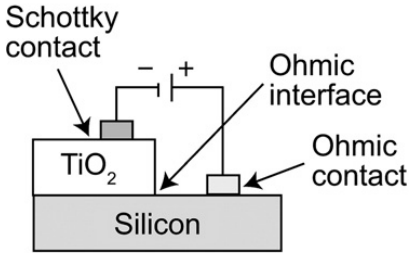


**Figure 3: Schematic of the Al/$TiO_2$/Si/Al Mott-Schottky diode test structure.**

### 2.3.2 Electrical Measurements

Electrical measurements are carried out on a probe station with four Signatone S-725 micropositioners, each connected to a dedicated 3 lug BNC triaxial cable for connection to instruments. Each micropositioner was equipped with a 1.25" SE-T tungsten probe tip with a tip diameter of 5.0 μm, and a shaft diameter of 25 mm. Measurement control and data collection were performed using a Shottky diode testing program within Agilent IC-CAP Device Modeling Software.

*I-V* sweeps were carried out using a Agilent B2900A Series Precision Source/Measure Unit. For a given sample, a sweep was taken using two Al/Si ohmic contacts to ensure that they demonstrated ohmic behavior and were of sufficiently low resistance. A typical sweep would be 400 data points from -0.5 V to 0.5 V. One of these contacts would be used in series with a $TiO_2$/Al contact for a second *I-V* sweep to demonstrate diode like behavior and determine the location of the diode's breakdown point under reverse bias. A typical sweep would be 800 data points from -10 V to 10 V with device breakdown typically occurring between -2 V and 2 V.

*C-V* sweeps were obtained using a Agilent E4980A Precision LCR Meter. Up to three $TiO_2$/Al contacts would be tested for each sample depending on the integrity and placement of the contacts. A typical sweep would be 500 data points between -1.5 V and 2.5 V with a frequency of 1 MHz. Two sweeps were obtained for

each sample. The first with is taken using default instrument settings with a "medium" integration time for each data point. The second increased the integration time to "long" and added a 5 ms hold at each data point. This later scan was to help ensure that scan data did not have any transient behavior caused by the rapidity of testing.

### 2.3.3 Carrier Concentration Determination

The extraction of carrier concentration values from *C-V* data is not trivial. Typical *C-V* sweeps can be divided into five regimes. On the two extremes, the device is in 'breakdown', which is to say that a sufficiently high voltage has been applied that the circuit ceases to act like a capacitor in series with a resistor and behaves like a series of resistors. In the middle behavior is divided into accumulation, depletion, and inversion regimes. Figure 4a shows a typical *C-V* plot for a $Al/TiO_2$ diode[2].

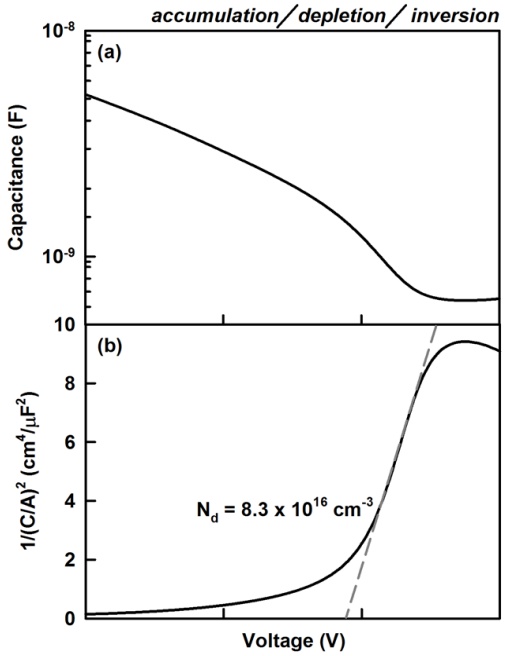


**Figure 4: a) C-V data and b) Mott-Schottky plots for a $Al/TiO_2$ device.**

In the accumulation regime (typically V<0), positive charges accumulate in the $TiO_2$ at the interface from the bulk. This coupled with a reduction in positive charge on the Al side produces a higher capacitance. In the depletion region ($0<V<V_{FB}$) the reverse occurs. Positive charges from the bulk Al are pushed to the interface while positive minority carriers in the $TiO_2$ are drawn away creating a negatively charged depletion layer at the $TiO_2$ side of the interface. These oppositely charged interface sides lower the capacitance. Inversion ($2V_{FB}<V$) occurs as negative charge carriers from the $TiO_2$ bulk are now pushed to interface increasing capacitance.

In the depletion region, the device obeys the Mott-Schottky Equation below.

$$\frac{1}{C^2} = \left( \frac{2}{q\varepsilon_0 \varepsilon N_D A^2} \right) \left( V - V_{FB} - \frac{kT}{q} \right) \qquad \text{(Equation 4)}$$

**Equation 4: Mott-Schottky Equation**

*C* is the capacitance across the semiconductor/metal interface, $\varepsilon_0$ is the permittivity of free space, $\varepsilon$ is the dielectric constant for the semiconductor ($\varepsilon_{TiO2}$ =55 [36]), *V* is the applied voltage, $V_{FB}$ is the flat band voltage, *kT/q* is the potential from thermal generation of electron hole pairs, *A* is the contact area, and $N_D$ is the net donor concentration. Equating net donor concentration and carrier concentration is valid for applied potentials which are low enough to form the generation of ions in the solid. $N_D$ can be extracted by plotting $1/C^2$ v. *V* and determining the slope in the depletion region as seen in Figure 4.

# Chapter 3

# EFFECT OF GROWTH RATE ON CARRIER CONCENTRATION

## 3.1 Introduction

During a CVD process, when precursors decompose leaving only the desired atoms on the surface, the deposited atoms will initially have high mobility on the free surface of the films. In the case of epitaxial or crystalline growth, these surface atoms should find a lattice site quickly and remain there to be covered by the subsequent layer of atoms. For amorphous growth, there is little need to promote this surface migration. Furthermore, for pseudo-ALD processes where more than a single atomic layer is deposited at a time, surface atoms may not be able to find an ideal site before being 'buried' by other atoms or having their lateral movement restricted by other deposited atoms.

Growth rate is known to have an influence on the appearance of the product film. In cases of very slow growth rates (~1 Å/cycle) polycrystalline films were grown well below 300 °C with no annealing needed[37]. Most ALD work produces amorphous films, but retains growth rates of 1 nm or less per cycle. When compared to other synthesis methods such as sol-gel where a liquid precursor is used, there is a great difference in growth rates with very little knowledge in the intermediate regime. Pseudo-ALD is still much lower than the growth rate achieved with a liquid precursor. Despite being self limiting, pseudo-ALD is also

fundamentally different than ALD because the growth is multiple atomic layers per cycle.

The pseudo-ALD regime was selected to test the effects of growth rate on film morphology and carrier concentration. Films in this regime are grown slowly enough to ensure complete precursor decomposition and uniform film growth. At the same time, films are grown quickly enough such that surface diffusion will be limited by subsequent atomic layers and therefore easily controllable by variation of precursor delivery rates.

### 3.2 Experimental Setup

Our chamber has the ability to control the rate of thin film deposition by controlling the duration of precursor pulses delivered to the chamber. This is the simplest method for varying precursor delivery as it is done within the Labview program. Other methods could include varying the $N_2$ carrier gas pressure or flow rate, but these would be much less precise and could introduce other problems such as TTIP vapor condensing in the line between the heated bubbler and the chamber.

Although the Labview program is designed to deliver layer by layer growth through alternating precursors, whether or not true ALD is achieved is only determined after the film is fully grown. Growth rate is calculated simply by dividing the thickness determined by ellipsometry and dividing by the number of cycles inputted by the user. Much of the work done in our group uses growth rates >> 1 Å/cycle; this range is considered to be far outside the regime of true ALD.

For this experiment, growth rates were varied from 4 Å/cycle to 7.5 nm/cycle and were grown to a thickness of 105 ± 5 nm with varying numbers of ALD

cycles at 200 °C. Samples were annealed at 550 °C for 24 hours with a ramp rate of 20 °C/min.

### 3.3 Hypothesis

As discussed earlier, there is a great deal of literature that deals with correlating improved photocatalytic reaction rates with changes in morphological properties. Typically, 'improved' material had a greater degree of crystallinity, avoided the formation of the rutile phase as well as amorphous, and had large grains with few pores.

A relationship between increased density and decreased carrier concentration seemed reasonable, and was tested through the variation of growth rate. During annealing, crystallization causes films to contract and become more dense as they become more ordered. It would follow that amorphous films deposited at slower rates would be more dense even in their amorphous state due to short range order. Deposited atoms would have more time to orient themselves relative to their neighbors before subsequent layers were added. These films would then contract less to their final polycrystalline density during annealing

Densification via short range order was not expected to significantly affect crystallinity as random nucleation during annealing is still expected to make up the majority of nuclei produced that are present as crystallites in the final film. The primary effect of the increase in bulk density is the reduction of inter-granular void space that formed during annealing leaving less surface area for oxygen vacancies to aggregate, thus lowering carrier concentration.

### 3.4 Morphological Characterization

Previous XRD work had shown no variation in crystallite size with changes in thickness and very little with long annealing times[2]. This does not give any implication as to variation in grain size or bulk density, but it remains consistent with the assumption of random nucleation in the sample near the beginning of annealing such that crystallite sizes should not change significantly once the sample is completely crystallized. The same work showed an increase in bulk density with annealing time and a decrease with thickness. This indicated that the film was compacting in some way though whether it involved removal of inter- or intra-grain void space in unknown. The formation of both types of void space has been documented in other crystalline materials due to the rapidity of grain growth[38, 39].

XRR and XRD were performed on each sample to determine both bulk density and crystallite size. XRD 2θ-Ω scans were taken over a range of 20° - 80° to encompass all easily discernable anatase peaks. This range also included several easily discernable rutile peaks as a means of detecting rutile formation. Quantification of anatase/rutile composition was not done as rutile components were typically very minor. Figure 5 shows minimal variation in anatase [101] peak intensity (2θ=25.281°) with growth rate. Error bars are uncertainties in crystallite size determination from the JADE software package based how well resolved the peak is.

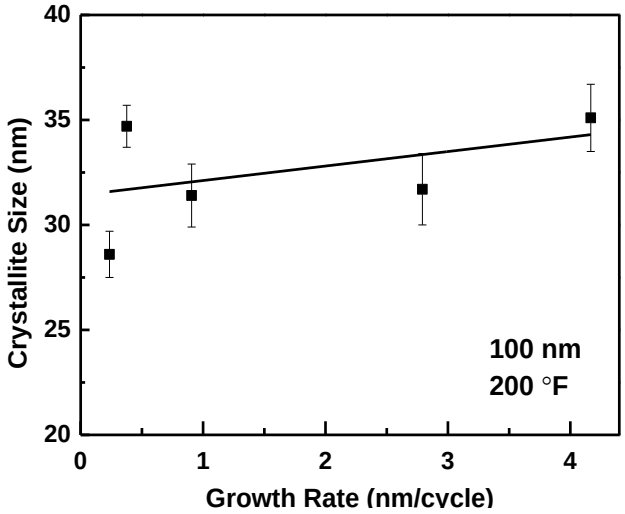


**Figure 5: Variation in Anatase [101] Crystallite Size with Growth Rate. Error bars taken from JADE peak fitting results. Fitted line is a linear least squares fit showing slight trend.**

Because of the minimal variation seen here, and changes in bulk density and carrier concentration would likely be more likely due to reduction in void space. The increased short range order at low growth rates producing more crystallites has a competing effect with bulk density. That is to say, increased bulk density removes inter-grain void space, but a larger number of small crystallites provides more intra-grain boundaries that are also more favorable for defect clustering than the bulk.

The variation in crystallite size seen for anatase [200] and [211] peaks ($2\theta$ = 48.05° & 55.061°) was less apparent. Because higher order refraction peaks were generally less well resolved, uncertainties also increased from ~1 nm to 5-10 nm. Similarly, data for density at 8 nm/cycle is not shown as the sample was both aged significantly and had a rough surface making accurate X-Ray based techniques difficult.

XRR $2\theta$-$\Omega$ scans were taken from 0.2° - 3° to encompass the critical reflection angle, as well as all discernable thickness fringes. Bulk density decreased with growth rate by about 10% over the range tested as seen in Figure 6. The single crystal density of anatase $TiO_2$ is 3.89 g/cm$^3$.

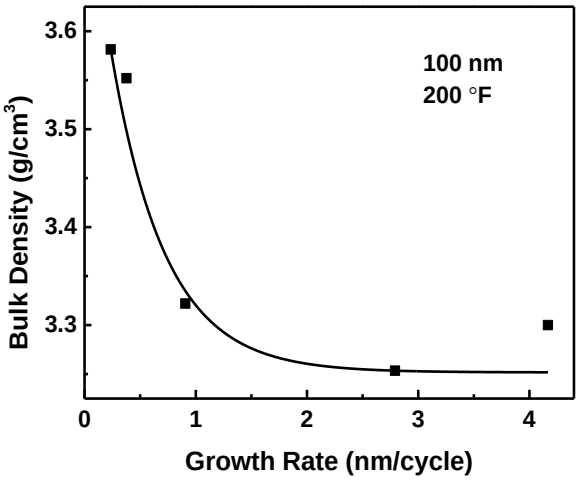


**Figure 6: Bulk Density v. Growth Rate. Fitted line is a least squares fit of an exponential function to be used as a guide for the eye.**

This suggests that there is a relation to final grain form or film porosity to the rate of growth even when the initial growth is amorphous. The sharp changes around 1 nm/cycle also lend credence to the hypothesis that the density change is linked to surface mobility of deposited atoms. Data for density at 8 nm/cycle is not shown as the sample was both aged significantly and had a rough surface making accurate X-Ray based techniques difficult. Films grown with a process more closely resembling ALD give deposited atoms time to move freely on the surface before the subsequent layer is added. Meanwhile, films that experience multiple atomic layers deposited at a time lose this advantage.

### 3.5 Electrical Characterization

Ohmic contacts and diodes were fabricated as described above. Depending on the quality of the diode contacts synthesized, up to three independent contacts on each sample were analyzed. Determination of depletion region was done by hand by looking for the linear regions of the Mott-Schottky plot ($C^{-2}$ v. $V$) and

fitting a linear regression to different numbers of points until $R^2$ error was minimized. The results can be found in Figure 7.

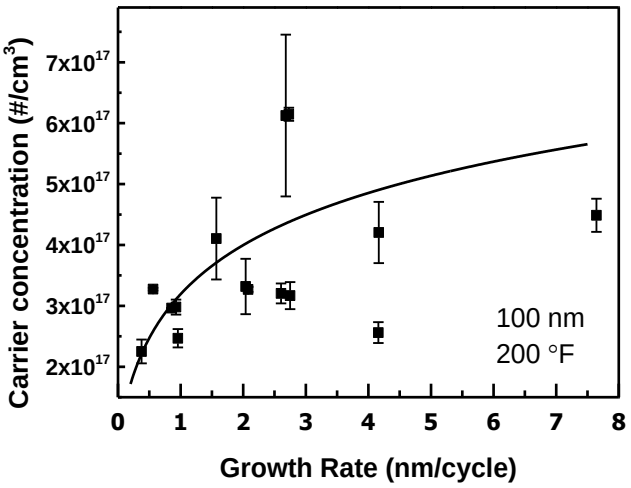


**Figure 7: Carrier Concentration v. Growth Rate. Fitted line is a logarithmic function fit of data up to 3 nm/cycle and is meant as a guide to the eye.**

The variation of about ½ an order of magnitude demonstrates the link between increased density and carrier concentration. Data points up to 3 nm/cycle were least-squares fitted to a logarithmic function meant as a guide to the eye. We do not have any *a priori* reason to expect a linear trend in this case and the fitted line may be treated as a simple guide for the eye. The leveling off above 3 nm/cycle has not been fully explained beyond the similar leveling off of density seen in Figure 6.

This result is consistent with previous work done in which films annealed for varied lengths of time saw little to no variation in crystallite size, further suggesting that the bulk of nucleation of crystallites in the amorphous film occurs before the 24 hold time of the anneal[2]. The question then becomes whether these crystallites are formed during the ramp up to 550 °C from room temperature, or whether they are present in the amorphous film, but are too small to be detected by conventional XRD.

The present work corroborates the presence of subcritical nuclei throughout the amorphous film as a means of explaining the lowering of carrier concentration with slower pseudo-ALD growth rates. If the crystallites were forming entirely upon annealing, some significant variation in crystallite size would have been expected, whereas the data in Figure 5 shows a minimal trend. Rather, the number of subcritical nuclei remained fairly static upon synthesis, but the improved density forced them closer together so as they grew, contact between them was improved leaving fewer grain boundaries with energetic conditions favorable to the clustering of oxygen vacancies. In addition to confirm the suspected presence of subcritical nuclei in the bulk, the manipulation of subcritical nuclei by varied synthesis rate represents a new tool to the field of defect engineering.

# Chapter 4

# EFFECT OF SYNTHESIS TEMPERATURE ON CARRIER CONCENTRATION

## 4.1 Introduction

Encouraged by the discovery of the effect of growth rate on carrier concentration, other means of increasing surface atom mobility were pursued. Similar to growth rate, the synthesis temperature used by various groups making $TiO_2$ thin films by CVD techniques has a lot of variation in the literature. Often no explanation is given for why a temperature is selected and the reader is left to assume the selected temperature is simply one used in the past by a given group and there is no desire to change a protocol that works. At low temperatures (~100 °C and below), surface mobility of Ti atoms has been shown to be a limiting factor in layer-by-layer growth[40]. While issues of film uniformity were solved by going to higher temperatures, this does not necessarily imply any changes to microstructure with temperature. Others have found changes in microstructure with variations in sputtering temperature for $TiO_2$ films[41]. Here, films sputtered at higher temperatures had increasing crystallite size but constant porosity suggesting that the effect of temperature was constrained to nanoscale crystalline quality, but not grain quality. Similar efforts were made using Plasma Enhanced ALD (PE-ALD) but comparisons are to make as films crystallized during growth at 250 °C rather than amorphous[16]. Similar difficulties are found with films grown using true ALD where films were able to crystallize well below 300 °C

during growth[17]. Effects of ALD temperature on photocatalysis have been documented as stated before, but lack in their ability to connect morphological variation and carrier concentration[19].

### 4.2 Experimental Setup

In order to test the effect of synthesis temperature on morphology, films were grown to thicknesses of 100 ± 5 nm at temperatures between 150 and 275 °C. Growth rate was nominally 1.5 nm/cycle with about 0.3 nm/cycle variation between samples. Pulse lengths were varied between temperature via the Labview program to keep growth rate similar. To determine the effect of temperature on carrier concentration, films were grown between 150 and 275 °C at rates of 1.5 ± 0.1 nm/cycle to thicknesses of 100 ± 5 nm. All samples were subjected to annealing at 550 °C for 24 hours with a ramp rate of 20 °C/min.

### 4.3 Hypothesis

The effect of improved surface mobility from increased temperature on carrier concentration was expected to match that of lowered growth rate. Giving surface atoms more energy to translate to sites of lower energy will compensate for the fact that the number of free surface atoms has increased at the same time. Similarly, increased energy (via temperature) should stimulate the production of subcritical nuclei within the amorphous film during growth. If so, a similar trend of increased density despite near constant (or slightly decreasing) crystallite size was expected with increasing temperature.

## 4.4 Morphological Characterization

The relationship between density and temperature was precisely as predicted. Increases in temperature produced samples with significantly higher density with the sample grown at 275 °C approaching the single crystal density of 3.89 g/cm$^3$. The results can be seen in Figure 8.

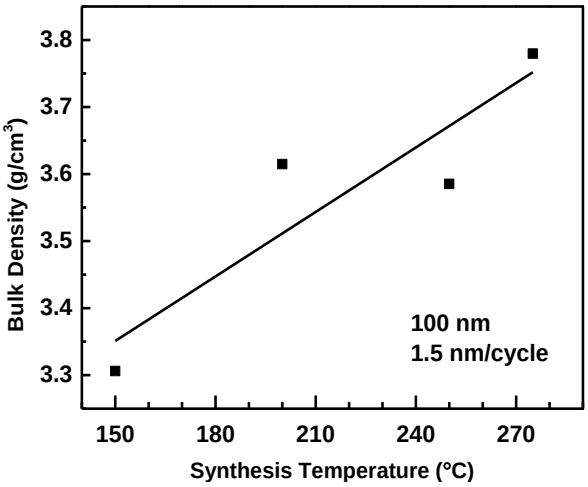


**Figure 8: Bulk Density v. Synthesis Temperature. Fitted line is a linear least-squares fit to the data; meant as a guide to the eye.**

Here the added line is a linear fit to the data. As with the varied growth rate data, there is no *a priori* reason to expect a linear trend. With such improvement in bulk density, it was assumed that there would be a slight drop in crystallite size with temperature as seen with samples of varying growth rates. This corroborates the theory that removal of porous space within the sample can be removed by the increased surface mobility of atoms during synthesis.

While the nominal crystallite size of 30 nm did not change significantly between the experiments, the expected trend was not apparent. A marginal improvement in crystallite size was seen with increasing synthesis temperature as seen in Figure 9.

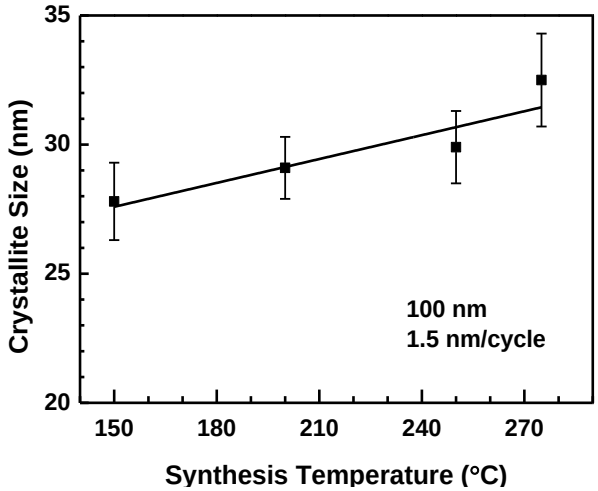


**Figure 9: Variation in Anatase [101] Crystallite Size with Synthesis Temperature. Fitted line is a linear least squares fit for use as a guide to the eye.**

Figures for the anatase [200] and [211] crystallite sizes are not shown for the same reasons as in the growth rate study. Relatively large and overlapping error bars nullify any seemingly apparent trend in the data. In the case of the better resolved [101] crystallite size, the increase with increased temperature lends some ambiguity as to the extent of short range order in an amorphous sample. It was argued that lower growth rates allowed for the formation of a greater number of subcritical nuclei in the sample. The same seamed reasonable for an increase in temperature; the data here seem to instead suggest an increase in the size of the subcritical nuclei allowing them to grow more rapidly upon annealing thus crowding out some of those formed during annealing.

Crystal growth is rapid once annealing temperatures are reached as temperature programmed XRD studies have shown with the first peaks clearly visible after about 20 minutes[2]. If a small number of crystallite seeds formed during synthesis, it would not be unreasonable to expect them to grow rapidly upon annealing possibly inhibiting further random seeding within the sample.

This explanation makes an allowance for new nucleation to occur during annealing regardless of the presence of subcritical nuclei. This is very reasonable as the total peak area in the temperature programmed XRD studies do not reach their maximum area for several hours indicating full conversion of amorphous material to polycrystalline anatase[2].

### 4.5 Electrical Characterization

Following annealing, samples were then patterned with aluminum contacts covering both an abraded silicon surface as well as the free $TiO_2$ surface. *I-V* and *C-V* sweeps were carried out as described earlier. Determined carrier concentrations can be seen in Figure 10.

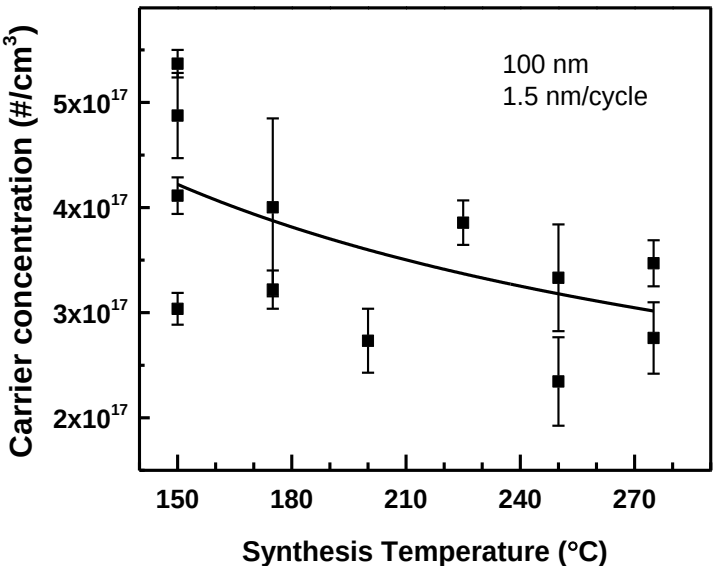


**Figure 10: Carrier Concentration v. Synthesis Temperature. Fitted power law curve is a guide to the eye, not based on an *a priori* argument.**

The trend is less pronounced as compared to the growth rate study, but there remains a clear trend towards lower carrier concentrations at higher temperatures. Here the fitting is a power law curve which was selected based on lower residual error than a

linear fit rather than any *a priori* arguments. The weakness of the trend can not be fully explained in the context of competing short range order and new nucleation upon annealing. Improved density and marginal gains in crystallite size at higher temperatures lead to lower carrier concentrations for the same reasons stated in Chapter 3. There is likely another temperature driven source of competition that is more apparent at higher temperatures. One explanation could be that at temperatures where surface mobility is no longer a limiting factor in growth, another source of active carriers aside from vacancy clusters at free surfaces develops. This would at least remain consistent with the idea of short range order in a seemingly amorphous film.

# Chapter 5

# EFFECT OF ANNEALING RAMP RATE ON CARRIER CONCENTRATION

## 5.1 Introduction

Complaints against the literature have already been made about the poorly explained link between growth conditions and catalytic performance[2]. There is an equally significant complaint to be made regard post growth processing. As stated earlier, even within the CVD and other layer-by-layer growth technique world (sputtering, PE-ALD), there is very little consistency amongst annealing conditions. Some groups claim to grow polycrystalline material from the outset[17] and either do not anneal, or anneal to further crystallization.

The vast majority grow amorphous films as we do and then anneal to form anatase material. The annealing is generally performed under an ambient atmosphere. There is great variation in the annealing temperature and hold time used[14, 19]. Anatase material typically starts to form between 300 °C and 400 °C. The rutile phase typically begins to form above about 650 °C. Both are however heavily time dependent. A sample annealed well below 650 °C will form rutile eventually and groups have reported growing anatase material below 300 °C without annealing but at very slow growth rates[16, 37]. Typical literature values vary from about 400 °C to about 600 °C with practically no discernable trend in total time. 24 hours was selected as an annealing time by our group as samples annealed for longer than 10 hours exhibited

less fluctuation or aging in carrier concentration afterwards despite the formation of anatase material after about 20 minutes[2].

While holding temperature and total annealing time are often reported, the ramp rate used to take a sample from either its synthesis temperature or room temperature to its annealing temperature is seldom reported. Under the assumption that nucleation continues (beyond the short range order already present) randomly throughout the sample, the temperature at which crystallization occurs is a critical piece of information.

### 5.2 Hypothesis

Given that our use of 550 °C as a final annealing temperature is well above the temperature required for anatase material to form, it is reasonable to assume that many if not the majority of the nuclei that form the basis for the final polycrystalline film have formed by the time 550 °C is reached. Though trends in density and crystallite size do not back the notion that crystallite size can be used as a proxy for grain size, a variation in crystallite size with annealing conditions would help to probe the idea of short range order forming in amorphous samples even before annealing.

We hypothesize that if the ramp rate used when annealing samples is slowed from a maximum of 1000 °C/min that carrier concentration will decrease. In this case, we expect a concurrent increase in crystallite size and density indicating that fewer larger crystallites make up each grain eliminating intra-grain space even if not inter-grain pores. This will reduce the area available for defects to cluster at free surfaces while improving overall crystallinity. The opposite trend would be expected for faster ramp rates.

This was tested by synthesizing films ranging from 50 to 300 nm at 200 °C at nominal growth rates of 2.5 nm/cycle. Films were then annealed at 550 °C for 24 hours following ramp rates of 20, 5 and 1 °C/min in the Barnstead furnace. An additional sample set was heated at a rate of 1000 °C/min (~17 °C/s) in the Jipelec RTP and held at 550 °C for 5 minutes. It was assumed that UV light was either not present or very minimal. Samples were cooled to room temperature over a period of approximately 3 minutes (samples then waited up to 15 minutes for other samples to undergo rapid thermal processing) before placement in the Lindberg tube furnace already at 550 °C and left for 24 hours. The 100 and 300 nm films annealed at 1 and 5 °C/min were selected for XRR and XRD analysis. The 100 nm films from the growth rate and temperature morphological studies were used for comparison to 20 °C/min. All films were electrically tested.

### 5.3 Morphological Characterization

The trend in crystallite size was much less pronounced than expected at low ramp rates. There were modest increases in crystallite size between the 1 and 20 °C/min samples, with the primary gains being between 20 and 1000 °C/min. In both cases, the [101] (Figure 11a) and [200] (Figure 11b) peaks were captured with great enough resolution to differentiate between samples.

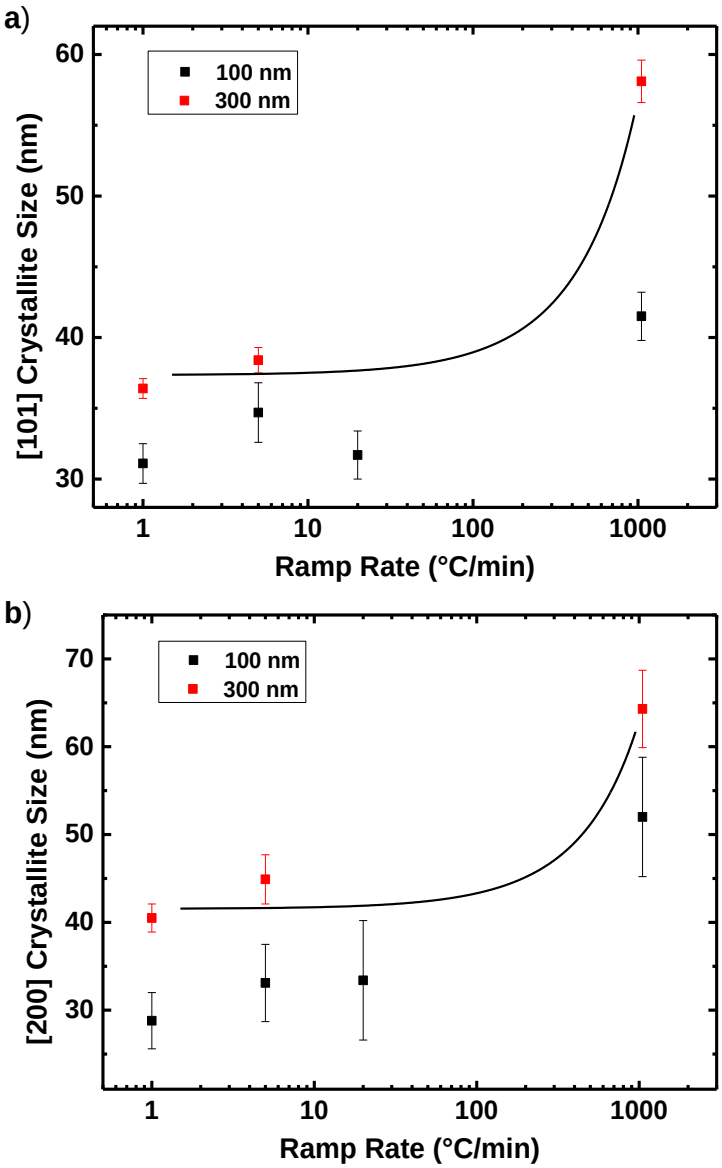


**Figure 11: Crystallite Size v. Annealing Ramp Rate for the a) [101] and b) [200] crystal faces. Error bars taken from JADE peak fit. Data at 20 °C/min taken from growth rate study (growth rate = 2.8 nm/cycle). Added lines are exponential fits of 300 nm data and are meant to be used as a guide for the eye.**

The overall trend is the reverse of expected with larger crystallites forming at faster ramp rates. This would indicate that new crystallite nucleus formation is slow relative to growth and that slowing the ramp rate beyond a critical point somewhere in the two orders of magnitude between 20 and 1000 °C/min allows a larger number of

crystallites to form which then can not grow as large. The exponential fitted lines were added to reflect this theory with little change at low ramp rates, and dramatic change above a transition point in the untested range. This is feasible given that the critical temperature for crystallite growth could be well below the hold temperature of 550 °C and slow ramp rates spend a significant portion of time (minutes to hours) between this temperature and the hold temperature; with a 1000 °C/min ramp rate, the time spent between any such critical temperature and the hold temperature would be less than 30 seconds.

A similar trend was seen in the density measurements. All of the samples that were annealed below 20 °C/min exhibited surface roughness above 1 nm which resulted in very poor resolution XRR data. As a result, the PANalytical X-ray Reflectivity software's curve modeling method was employed for density calculations for all samples. The values obtained can be seen in Figure 12. The fitted line is intended to be a guide to the eye and is not based on any *a priori* arguments. Data from Sellers *et al.* was acquired from Figure 3.5e using OriginPro's Digitizer function[2].

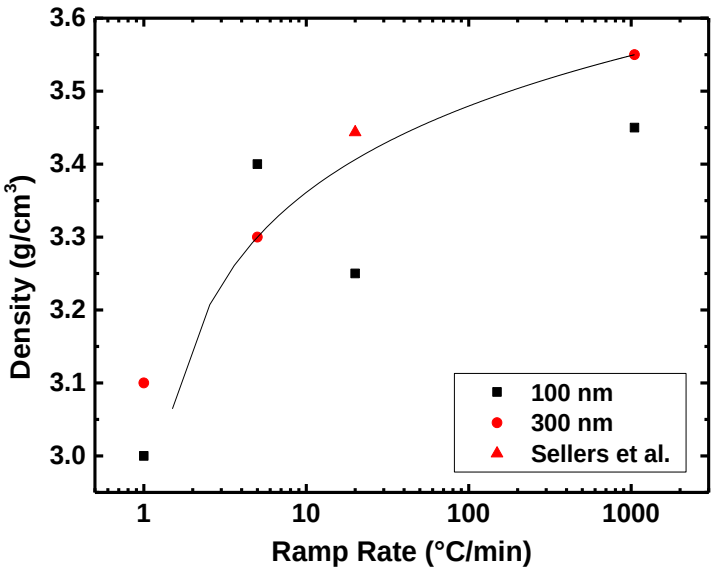


**Figure 12: Bulk Density v. Annealing Ramp Rate. 100 nm data at 20 °C/min taken from growth rate study (growth rate = 2.8 nm/cycle). Sellers *et al.*[2] 20 °C/min data point had a thickness of 251 nm. Added line is a logarithmic fit of the 300 nm data as a guide for the eye.**

The trend towards higher density at faster ramp rates is significant across the range accessed. The data do not suggest any reason for significantly increase surface roughness. The data in Figure 12 are consistent with the picture painted by the trend in crystallite size with regards to the presence of an unknown and competing temperature effect similar to that seen in Figure 8 and Figure 9. In these cases, increased crystallite size and increased density were observed with increased synthesis temperature and ramp rate respectively. Rapid annealing is likely allowing less time for new nuclei formation during the portion of the ramp up period where temperature is above a critical point for significant nuclei formation.

### 5.4 Electrical Characterization

Following annealing and morphological characterization, samples were patterned with aluminum contacts as described previously. Unlike the morphological characterization results, trends were negligible as seen in Figure 13.

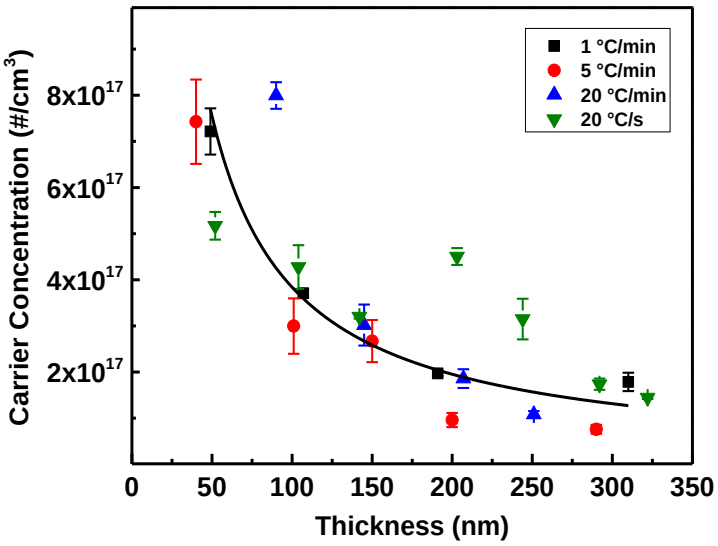


**Figure 13: Carrier concentration v. annealing ramp rate. Fitted curve is a best fit power law of the 1 °C/min data, for use as a guide to the eye.**

The best fit line is meant to be used as a guide to the eye and is not bases on any *a priori* arguments though the trend does match that observed in previous studies[2, 34]. Over the three orders of magnitude tested here, there is no apparent effect of ramp rate on carrier concentration. Data exhibit the same trend of decreasing carrier concentration with thickness seeing previously[2] each covering over approximately the same range with the same exponential decay at the highest thicknesses. If indeed fewer and larger nuclei are present in the final film at higher ramp rates, carrier concentration would be lower with increased ramp rate assuming that the grains are in good electrical contact removing space available for defect aggregation. More than likely, the lack of a trend is due to more than poor conductivity at grain boundaries.

Coupled with observed morphological changes there are several possible explanations. The first is the effects that short range order have on the final polycrystalline film materialize almost completely before the hold at 550 °C. Simply put, this entails the primary transition of subcritical nuclei to stable and growing nuclei during the ramp up but on a time scale almost too rapid for our RTP apparatus to

access. This explains this increase in density and crystallite size while allowing for little change is contact between the grains resulting in no change in carrier concentration

When observed in the context of enhanced surface diffusion, subcritical nuclei transformed to stable crystallites between approximately 200 and 300 °C[3]. The transition temperature for bulk $TiO_2$ would be expected to be close and well below the hold temperature of 550 °C used in the current work. The previous work also noted an induction time of 7.5 minutes for grain growth to be detectable by SEM[3]. This is less than half the time for TP-XRD to resolve crystallization in the bulk. A transition between instability and growth in amorphous $TiO_2$ could easily be on the order or milliseconds or shorter which RTP cannot access. If RTP was accessing the slower end of that range, it could explain the significant morphological differences at 1000 °C/min verses the lower 2 orders of magnitude, while suggesting that grain boundary formation during the hold remains dominant with regard to oxygen vacancy aggregation.

In a similar vein, a second explanation is that the formation of new crystallites by random seeding only occurs significantly during the hold and in late stages of slower ramp ups. This explanation is also feasible given the tendency for anatase to be visible by TP-XRD after 20 minutes of holding at 550 °C (following a 20 °C/min ramp up) and the common trend in the literature of forming anatase quickly at a variety of temperatures. It is possible this explanation is concurrent with the first.

A third explanation is that both significant growth of subcritical nuclei and significant formation of new nuclei are present during ramp up but with negligible temperature dependence. This is the less likely given that nucleation and crystallite

growth phenomena often have very strong temperature dependence. Before the 7.5 and 20 minute induction times were noted for surface and bulk $TiO_2$, induction time on an even shorter time scale had already been reported for surface silicon. Here, induction times at temperatures above 600 °C decreased from about 90 to 10 seconds over a range of 30 °C when grown by CVD[42]. No induction time was reported for the crystallization of amorphous silicon grown by Molecular Beam Epitaxy between 500 and 600 °C[43].

The fourth is that the first three explanations are overshadowed by the long anneal time and transient effects are overcome as the film reforms over time to a similar final state regardless of the initial state of crystallite seeds. This has some basis as it was reported previously that films annealed for shorter times (20 minutes) did exhibit some transient carrier concentrations values on the time scale of weeks to months[2]. This is similarly unlikely given the history of film stability with regards to reflecting growth conditions as seen in Figure 7 and Figure 10.

# Chapter 6

## CONCLUSIONS

We have for the first time offered significant evidence of the presence of short range order in amorphous $TiO_2$, likely in the form of subcritical nuclei. Their formation can be enhanced by increasing surface mobility of deposited atoms during deposition. Their presence has direct effects on the final morphology of annealed anatase films with regard to crystallite size and density. Increasing their presence has the desired effect of lowering electrically active carrier concentration by approximately ½ an order of magnitude over the ranges tested. Their competing relationship with other random nuclei formed through random seeding during annealing remains unclear as the effects of ramp rate on carrier concentrations are negligible suggesting crystal growth on a time scale currently inaccessible to us.

## REFERENCES


**1.** ONG SWD. *DESIGN OF BAND-ENGINEERED PHOTOCATALYSTS USING TITANIUM DIOXIDE*. Urbana: Chemical and Biomolecular Engineering, University of Illinois; 2013.

**2.** Sellers MCK. *DEFECT ENGINEERING OF POLYCRYSTALLINE TITANIUM DIOXIDE SYNTHESIZED BY ATOMIC LAYER DEPOSITION*. Urbana: Chemical and Biomolecular Engineering, University of Illinois; 2011.

**3.** Kondratenko YV, Seebauer EG. Directed self-assembly by photostimulation of an amorphous semiconductor surface. *AIChE.* 2010;56(12):3206-3211.

**4.** Londos CA, Sgourou EN, Chroneos A. Impact of isovalent defect engineering strategies on carbon-related clusters in silicon. *Journal of Materials Science: Materials in Electronics.* 2013;24(5):1696-1701.

**5.** Oliviero E, David ML, Fichtner PFP, Beaufort MF, Barbot JF. Lithium implantation at low temperature in silicon for sharp buried amorphous layer formation and defect engineering. *Journal of Applied Physics.* 2013;113(8):083515-083517.

**6.** Ronning C, Borschel C, Geburt S, Niepelt R. Ion beam doping of semiconductor nanowires. *Materials Science and Engineering: R.* 2010;70:30-43.

**7.** Lorenz K, Nogales E, Miranda SMC, et al. Enhanced red emission from praseodymium-doped GaN nanowires by defect engineering. *Acta Materialia.* 2013;61(9):3278-3284.

**8.** Chang H, Sun Z, Saito M, et al. Regulating Infrared Photoresponses in Reduced Graphene Oxide Phototransistors by Defect and Atomic Structure Control. *ACS Nano.* 2013/07/09 2013.

**9.** Yang P, Li X, Zhao Y, Yang H, Wang S. Effect of triangular vacancy defect on thermal conductivity and thermal rectification in graphene nanoribbons. *Physics Letters A.* 2013.

**10.** Kim S, Lee D, Park J, et al. Defect engineering: reduction effect of hydrogen atom impurities in HfO2-based resistive-switching memory devices. *Nanotechnology.* 2012;23(32):325702.

**11.** Bak T, Bogdanoff P, Fiechter S, Nowotny J. Defect engineering of titanium dioxide: full defect disorder. *Advances in Applied Ceramics: Structural, Functional & Bioceramics.* 2012;111(1/2):62-71.

**12.** Fujishima A, Honda K. Electrochemical Photolysis of Water at a Semiconductor Electrode. *Nature.* 1972;238(5358):37-38.
**13.** Hanaor DH, Sorrell C. Review of the anatase to rutile phase transformation. *Journal of Materials Science.* 2011;46(4):855-874.
**14.** Pore V, Kivela T, Ritala M, Leskela M. Atomic layer deposition of photocatalytic TiO2 thin films from TiF4 and H2O. *Dalton Transactions.* 2008;0(45):6467-6474.
**15.** Methaapanon R, Bent SF. Comparative Study of Titanium Dioxide Atomic Layer Deposition on Silicon Dioxide and Hydrogen-Terminated Silicon. *The Journal of Physical Chemistry C.* 2010;114(23):10498-10504.
**16.** Lee C-S, Kim J, Gu GH, et al. Photocatalytic activities of TiO2 thin films prepared on Galvanized Iron substrate by plasma-enhanced atomic layer deposition. *Thin Solid Films.* 2010;518(17):4757-4761.
**17.** Pheamhom R, Sunwoo C, Kim D-H. Characteristics of atomic layer deposited TiO2 films and their photocatalytic activity. Paper presented at: THE 52ND INTERNATIONAL SYMPOSIUM OF AVS, 2006.
**18.** Heikkilä M, Puukilainen E, Ritala M, Leskelä M. Effect of thickness of ALD grown TiO2 films on photoelectrocatalysis. *Journal of Photochemistry and Photobiology A: Chemistry.* 2009;204(2-3):200-208.
**19.** Cheng H-E, Hsu C-M, Chen Y-C. Substrate Materials and Deposition Temperature Dependent Growth Characteristics and Photocatalytic Properties of ALD TiO2 Films. *Journal of The Electrochemical Society.* August 1, 2009 2009;156(8):D275-D278.
**20.** Pickup DM, Sowrey FE, Drake KO, Smith ME, Newport RJ. New insights into medium-range order around titanium in solâ€“gel derived silica through isotope difference neutron diffraction and reverse Monte Carlo modelling. *Chemical Physics Letters.* 2004;392:503-507.
**21.** Lee B-S, Bishop SG, Abelson JR. Fluctuation Transmission Electron Microscopy: Detecting Nanoscale Order in Disordered Structures. *ChemPhysChem.* 2010;11(11):2311-2317.
**22.** Lee B-S, Burr GW, Shelby RM, et al. Observation of the Role of Subcritical Nuclei in Crystallization of a Glassy Solid. *Science.* 2009;326(5955):980-984.
**23.** Moona S-ICC-HCSH. Temperature-Programmed Desorption Study on the Decomposition Mechanism of Ti(OC3H7)4 on Si(100). *Journal of The Electrochemical Society.* 2001;148(9):C599-C603.
**24.** Duminica FD, Maury F, Hausbrand R. Growth of TiO2 thin films by AP-MOCVD on stainless steel substrates for photocatalytic applications. *Surface and Coatings Technology.* 2007;201(22-23):9304-9308.
**25.** Rahtu A, Ritala M. Reaction Mechanism Studies on Titanium Isopropoxide–Water Atomic Layer Deposition Process. *Chemical Vapor Deposition.* 2002;8(1):21-28.

**26.** Cho S-I, Chung C-H, Moon SH. Surface decomposition mechanism of Ti(OC3H7)4 on a platinum surface. *Thin Solid Films.* 2002;409(1):98-104.
**27.** Tuan A, Yoon M, Medvedev V, Ono Y, Ma Y, Rogers Jr JW. Interface control in the chemical vapor deposition of titanium dioxide on silicon(100). *Thin Solid Films.* 2000;377-378:766-771.
**28.** Aarik J, Aidla A, Uustare T, Ritala M, Leskel¨a M. Titanium isopropoxide as a precursor for atomic layer deposition: characterization of titanium dioxide growth process. *Applied Surface Science.* 2000;161(3-4):385-395.
**29.** Xie Q, Musschoot J, Deduytsche D, et al. Growth Kinetics and Crystallization Behavior of TiO2 Films Prepared by Plasma Enhanced Atomic Layer Deposition. *Journal of The Electrochemical Society.* September 1, 2008 2008;155(9):H688-H692.
**30.** Fictorie CP, Evans JF, Gladfelter WL. Kinetic and mechanistic study of the chemical vapor deposition of titanium dioxide thin films using tetrakis-(isopropoxo)-titanium(IV). Paper presented at: The 40th National Symposium of the American Vacuum Society, 1994; Orlando, Florida (USA).
**31.** Zhang Q, Griffin GL. Gas-phase kinetics for TiO2 CVD: hot-wall reactor results. *Thin Solid Films.* 1995;263(1):65-71.
**32.** Bergese P, Bontempi E, Depero LE. A simple solution to systematic errors in density determination by X-ray reflectivity: The XRR-density evaluation (XRR-DE) method. *Applied Surface Science.* 2006;253(1):28-32.
**33.** Holy V, Pietsch U, Baumbach T. *High Resolution X-ray Scattering from Thin Films and Multilayers*. New York: Springer; 1999.
**34.** Sellers MCK, Seebauer EG. Measurement method for carrier concentration in TiO2 via the Mott-Schottky approach. *Thin Solid Films.* 2011;519(7):2103-2110.
**35.** Li SS. *Semiconductor Physical Electronics*. New York: Plenum Press; 1993.
**36.** Enache C, Schoonman J, Krol R. The Photoresponse of Iron- and Carbon-Doped TiO2 (Anatase) Photoelectrodes. *Journal of Electroceramics.* 2004;13(1-3):177-182.
**37.** Kim SK, Hoffmann-Eifert S, Reiners M, Waser R. Relation Between Enhancement in Growth and Thickness-Dependent Crystallization in ALD TiO2 Thin Films. *Journal of The Electrochemical Society.* 2011;158(1):D6-D9.
**38.** Akther Hossain AKM, Rahman MA, Farhad SFU, Vilquin B, Tanaka H. Effect of Li substitution on the magnetic properties of LixMg0.40Ni0.60â^'2xFe2+xO4 ferrites. *Physica B: Condensed Matter.* 2011;406(8):1506-1512.
**39.** Kupecz JA, Gluyas JG, Bloch S. *Reservoir Quality Prediction in Sandstones and Carbonates: An Overview* American Association of Petroleum Geologists; 1997.

**40.** Sladek KJ, Herron HM. Titanium Dioxide Coatings. Room Temperature Deposition. *Product R&D.* 2013/07/08 1972;11(1):92-96.

**41.** Wang H, Wang T, Xu PEI. Effects of substrate temperature on the microstructure and photocatalytic reactivity of TiO2 films. *Journal of Materials Science: Materials in Electronics.* 1998;9(5):327-330.

**42.** Llera-Hurlburt D, Dalton AS, Seebauer EG. Temperature-dependent surface diffusion parameters on amorphous materials. *Surface Science.* 2002;504:244-252.

**43.** Sakai A, Tatsumi T, Ishida K. Growth kinetics of Si hemispherical grains on clean amorphous-Si surfaces. *Journal of Vacuum Science & Technology A.* 1993;11(6):2950-2953.